Journal of Corrosion and Materials
www.corromat.com

J. Corros. Mater. (2026) 5(1), 140–150.

Ultraviolet-Regulated Product-Layer Compactness and Sulfite-Sulfate Failure of Zn–Al–Mg Coated Steel during Extremely Cold Polluted Atmospheric Cycling

Jhon Jairo Fernández Hincapié[1,*]

Institute of Chemistry, Faculty of Exact and Natural Sciences, Universidad de Antioquia, Antioquia, Colombia

*Corresponding author: john.fernandez@udea.edu.co

(Received: 18 March 2026. Received in revised form: 30 May 2026. Accepted: 12 June 2026. Published online: 30 June 2026.)

Abstract

The influence of ultraviolet illumination on corrosion rate, surface film tightness, crystalline conversion, and defect density in Zn–Al–Mg coated steel under an extremely cold polluted atmosphere was investigated. The coating metal consisted of ∼20 μm thickness with composition of 4.4 wt.% Mg, 6.8 wt.% Al, 4.8 wt.% Si, 0.5 wt.% P, and balance Zn. The test atmosphere consisted of cycles of cooling to −60 °C, heating to 20 °C, humidity control to 95% relative humidity, and drying for 12 h daily. Deposition rate of sodium bisulfite was 5.09 mg cm^{-2} d^{-1} each 7 day, whereas ultraviolet illumination at wavelength of 340 nm and power of 5 W m^{-2} was applied continuously throughout testing duration. Measurement techniques employed included gravimetric measurement, electrochemical impedance spectroscopy, in-situ impedance measurement, x-ray diffraction, scanning electron microscopy, and Mott-Schottky analysis to correlate rate with surface-film continuity and defect-mediated ion permeation. The rate of corrosion after 7 days was negligible, but dark exposure caused greater mass loss compared with that exposed to ultraviolet light from days 14 to 35. The effect of ultraviolet illumination inhibition fell from 25.7% at day 14 to 11.2% at day 35, showing that ultraviolet irradiation provided only a temporary barrier improvement. The polarization resistance was achieved to be 2.36×10^4 Ω cm^2 in dark after 21 days and to be 4.80×10^4 Ω cm^2 under ultraviolet illumination after 14 days. X-ray diffraction confirmed no formation of a new crystalline compound by ultraviolet illumination but a delay in converting $Zn_4SO_4(OH)_6{\cdot}4H_2O$-dominated products to $Zn_2(SO_3)(SO_4){\cdot}3H_2O$ products. Observation under scanning electron microscope revealed a thickness of 3.77 μm loosely packed products after 7 days in dark while thickness under ultraviolet illumination condition was lower at 1.93 μm. Mott–Schottky analysis verified n-type products and revealed a reduction of donor density from 1.65×10^{20} cm^{-3} without ultraviolet illumination to 4.88×10^{19} cm^{-3} under ultraviolet illumination. In conclusion, the coating behavior resulted from two major mechanisms namely ultraviolet illumination enhanced hydroxysulfate product layer densification and conversion of sulfate products to sulfite products by sodium bisulfite deposition with resultant freeze-thaw cracking.

Keywords: Zn–Al–Mg coated steel; atmospheric corrosion; ultraviolet illumination; sodium bisulfite; freeze-thaw cycling; electrochemical impedance spectroscopy; Mott–Schottky analysis.

1. Introduction

Zn–Al–Mg coated steels have applications in situations where zinc-based coatings need to protect structural steels in a corrosive environment characterized by wetness, exposure to pollution, and cyclic exposure conditions. Such coatings provide protective function via mechanical isolation of the steel surface, dissolution of zinc-rich sites, and precipitation of corrosion products able to block oxygen and electrolyte access. The coating layer is not homogenous chemically but involves magnesium and aluminum alloying that impacts microstructure, galvanic activity, corrosion-product solubility, and product adhesion. Zn–Al–Mg coatings can form protective product layers superior to conventional galvanized zinc under suitable exposure conditions [1]. Corrosion-product characterization of Zn–Mg–Al coated steel confirms that alloying affects the nature and compactness of the surface layer [2]. Atmospheric-exposure studies also show that Zn–Al–Mg coatings can outperform standard zinc coatings when corrosion products remain protective [3]. Additional long-term exposure work supports the role of product-layer continuity in protection [4]. Marine-atmosphere characterization further confirms that corrosion products on Zn–Mg–Al coated steels depend on the local environment [5]. Worldwide weathering studies show that long-term atmospheric performance depends on exposure site and coating chemistry [6]. Accelerated and natural-exposure studies identify electrolyte composition as a key factor in corrosion-product formation [7]. Complementary work shows that Mg and Al alloying changes the formation and properties of corrosion products in different electrolytes [8]. Initial corrosion studies in extremely cold industrial climates confirm the importance of evaluating Zn–Al–Mg coatings under severe atmospheric conditions [9]. Thus the performance of the zinc-based coating is not determined by the existence of the layer itself but by the compactness and continuity of the product layer.

The process of atmospheric corrosion develops due to reactions proceeding within thin layers of electrolytes produced by condensation of moisture, melting of snow, deliquescence of salts, retained moisture, and pollution. Early atmospheric-corrosion analysis explains how thin electrolyte films govern outdoor metal degradation [10]. Zinc dissolution, oxygen

reduction, pH changes, and precipitation of corrosion products occur inside this limited surface film. Zinc-corrosion studies further show that oxides, hydroxides, carbonates, sulfates, and related products can change the transport properties of the surface layer [11]. Atmospheric-corrosion modelling also stresses the role of wetness, pollutant retention, and transport through the product layer [12]. Comprehensive treatments of atmospheric corrosion confirm that compact products may restrict mass transfer, whereas porous products may retain electrolyte and support further attack [13]. The distinction is especially significant in case of Zn-Al-Mg coatings since magnesium and aluminum impact the precipitation and, thus, the stability of the hydroxy-sulfate and sulfate-sulfite products.

An extreme temperature environment increases the complexity of atmospheric corrosion. Low temperatures affect kinetic parameters of the corrosion reactions but do not stop the process if wet surfaces, polluted snow and air, and freeze-thaw cycles are involved. Repeated transitions between frozen, humid, dried, and contaminated states of the metal surface take place in such climatic conditions. Mikhailov et al. pointed to the significance of wetness and pollutant retention in low-temperature corrosion [14]. Welded steels suffer under arctic maritime exposure [15], and extreme temperature changes at −60 °C negatively affect protective coating systems [16]. Therefore, Zn-Al-Mg coatings under cold-industrial atmosphere require examination under multiple temperature and humidity variations along with pollutant exposure and UV radiation.

Sulfur-containing pollutants are vital for understanding the studied corrosion. Species of bisulfite, sulfite, and sulfate are accumulating on cold surfaces and becoming concentrated as a consequence of evaporation. Zinc hydroxy-sulfate, $Zn_4SO_4(OH)_6{\cdot}4H_2O$, is a known atmospheric zinc corrosion product that can contribute to protection when it precipitates into dense layers [17]. Additional zinc-atmosphere studies confirm that sulfate-containing corrosion products may influence surface-layer stability [18]. In case of ZnAlMg-coated steel, SO_2-based atmospheric corrosion causes formation of corrosion products regulated by pH and microstructural activity [19]. As a result, sodium bisulfite is an essential source of sulfur-containing compounds, participates in acidification of the electrolyte and drives conversion of the hydroxy-sulfate corrosion products to hydrated sulfate-sulfite products.

Exposure to ultraviolet illumination introduces another factor, which relates to the electronic properties of zinc oxides and hydrated zinc corrosion products. Illumination may change charge carriers' population, alter surface potential, modify oxygen reduction rate, and affect the defect density of corrosion products. Semiconductor band-position data explain why oxide and mineral corrosion products may respond differently to illumination [20]. Zinc photo-corrosion has been reported in neutral solutions [21]. Ultraviolet light can also affect atmospheric corrosion in chloride-containing electrolytes [22]. Illumination influences passive-film stability on some metals through changes in the electronic state of the surface film [23]. Related photoelectrochemical studies show that passive-film response depends on defect structure and charge-carrier behavior [24]. Additional work confirms that light effects are system dependent across different passive and semiconducting films [25]. Electrochemical analysis of corrosion products on Zn–Mg, Zn–Al, and Zn–Al–Mg coatings further supports the need to connect film chemistry with measured surface response [26]. In the same way, ultraviolet exposure cannot be assumed beneficial or adverse to corrosion performance, but it is system dependent, and its effect should be related to product formation on the coating.

In this paper, Zn-Al-Mg-coated steel will be examined after being subjected to several cycles of cooling to −60 °C, humidification, drying, deposition of sodium bisulfite, and ultraviolet irradiation. The scientific question is whether ultraviolet exposure increases the protective function of the layer by affecting the crystalline form of the product, compactness of the layer, and semiconductor defects. The answer to the posed question is achieved based on corrosion loss measurements, ex-situ impedance spectroscopy, in-situ impedance spectroscopy, X-ray diffraction analysis, scanning electron microscopy and image analysis, and Mott-Schottky measurements. The figures included in the manuscript are arranged according to the experimental process and measured data: coating type, test cycle, corrosion loss, impedance behavior, conversion of the product layer, product compactness, initial pollution response, semiconductor defect density, final cracking, and concluding evidence.

2. Materials and Methods

2.1 Coating material and sample preparation

The sample used was Zn-Al-Mg coated steel having a metallic coating thickness of about 20 μm. Compositionally, the coating consisted of 4.4 wt.% Mg, 6.8 wt.% Al, 4.8 wt.% Si, 0.5 wt.% P and the remaining of Zn. The corrosion surface was the coated side of the specimen, while the steel substrate remained underneath the metallic coating. It is evident from the section and composition given in Figure 1 that corrosion reaction can no longer be assumed to involve only zinc dissolution. Magnesium and aluminum can influence local acidity and precipitation properties, while the zinc-rich base metal provides zinc ions necessary for zinc hydroxy-sulfate and zinc sulfate sulfite.

The coupons measuring 50 mm × 50 mm × 1.54 mm were prepared by cleaning the test surfaces using acetone and



Figure 1: Coating section and composition of the Zn-Al-Mg coated steel.

alcohol. All cut edges were taped to minimize the edge effect and assure accurate response only from the coated surface. Four specimens were prepared for each exposure time. Three specimens served as test pieces for determination of mass loss, while one specimen was prepared for analysis of corrosion morphology, phases and electrochemistry. Corrosion products were removed from the surface at ambient temperature using saturated glycine solution during 1–10 min as per ISO 8407 standard [27]. Dried coupons were weighed by analytical balance.

For electrochemical experiments, test pieces measuring 1 cm^2 were cut out by means of polytetrafluoroethylene tape, rosin paraffin and copper conductor. Impedance spectroscopy measurements were done using comb electrodes measuring 30 mm × 30 mm with an electrode separation of about 277.51 μm. This setup enabled observation of early stages of the corrosion process prior to the dominating phenomena of mass loss and cracking.

2.2 Cyclic extremely cold polluted exposure

Cyclic accelerated exposure was conducted in a climate chamber in dark and ultraviolet light conditions. Each cycle was composed of cooling down from 20°C to -60°C in 2.5 hours, holding at -60°C for 4 hours, re-heating from -60°C to 20°C in 2.5 hours, humid environment at 20°C and 95% relative humidity for 1 hour, and drying at 20°C for 2 hours. Sodium bisulfite was added at 5.09 mg cm^{-2} d^{-1} in each seventh cycle. The ultraviolet exposure was performed at 340 nm wavelength and 5 W m^{-2} power. Sampling was done at 7, 14, 21, 28, and 35 days. Time-resolved exposure cycle shown in Figure 2 presents cyclic extreme cold bisulfite exposure with thermal, humidity, drying, pollutant, and ultraviolet stages.

The above described exposure cycle is important since corrosion products generated during one stage of this exposure can be influenced during others. For example, humidity provides electrolyte for zinc dissolution and oxygen reduction processes. Drying enhances solubility of bisulfite, sulfite, and sulfate ions. Cooling and re-heating processes cause stress on the hydrated corrosion layer, producing discontinuity on its surface. The use of both dark and ultraviolet irradiation isolates effect of illumination while keeping the same thermal and chemical conditions.

2.3 Phase, morphology, and electrochemical characterization

Surface and cross-sectional morphologies were observed by environmental scanning electron microscope with energy dispersive spectroscopy analysis. Samples were mounted in epoxy resin, ground up to 2000 grit size, and polished with 2.5 μm diamond pastes. X-ray diffraction was done with Cu Kα radiation at 40 kV and 40 mA for 2θ angle between 4° and 90°.

Electrochemical tests were carried out with PARSTAT 2273 electrochemical workstation. Corroded Zn-Al-Mg sample served as the working electrode. Platinum wire and saturated calomel electrode were counter and reference electrodes respectively. Experiments were performed with 0.1 mol L^{-1} Na_2SO_4 solution at potential stabilization. Impedance spectra

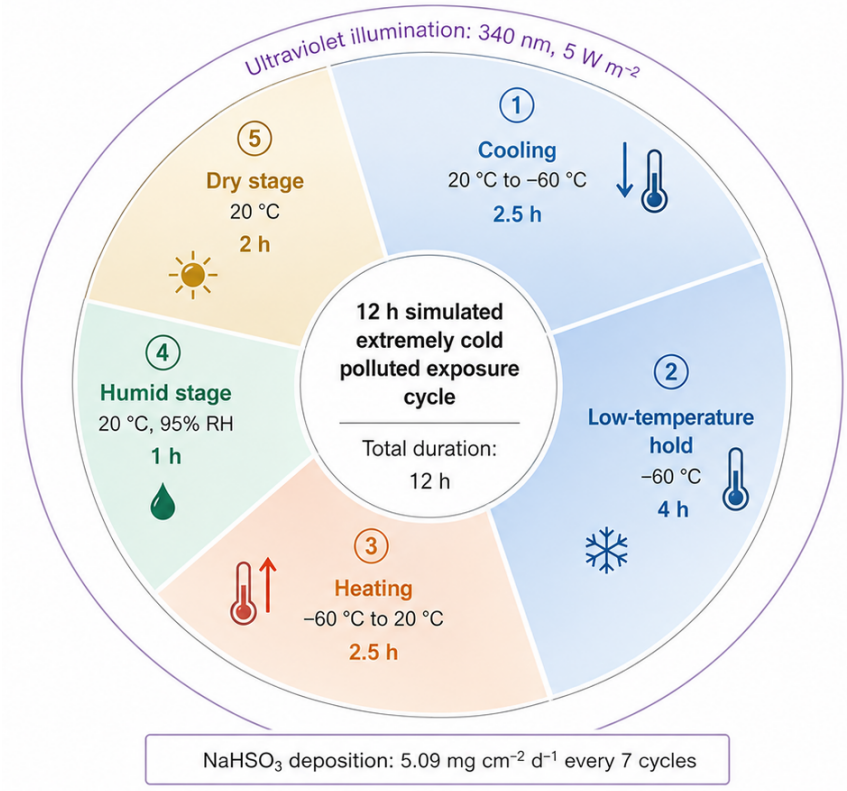


Figure 2: Twelve-hour extremely cold bisulfite exposure cycle.

were measured at open-circuit potential with 10 mV amplitude and 10^5 to 10^{-2} Hz frequency. Mott-Schottky curves were done at 1 kHz from -1.5 to -2.1 V in steps of 50 mV.

Inhibition efficiency due to ultraviolet exposure was calculated as

$$\eta_{\mathrm{UV}} = \frac{D_{\mathrm{dark}} - D_{\mathrm{UV}}}{D_{\mathrm{dark}}} \times 100\%, \tag{1}$$

where D_{dark} and D_{UV} correspond to mass loss in dark and ultraviolet environments respectively. This quantity is determined by development, transformation, and cracking of the product layer.

For interpretation of electrochemical impedance spectra the equivalent circuit consisted of solution resistance (R_s), corrosion-product resistance (R_r), product-layer constant phase element (Q_r), charge transfer resistance (R_{ct}), and double-layer constant phase element (Q_{dl}). Polarization resistance was calculated as

$$R_p = R_r + R_{ct}. \tag{2}$$

R_r characterizes resistance in product layer, whereas R_{ct} characterizes resistance to charge transfer at coating/electrolyte interface. High value of polarization resistance therefore demands compact structure of product layer and low activity at coating/electrolyte interface.

Analysis of Mott-Schottky curves was performed as follows:

$$\frac{1}{C^2} \approx \frac{1}{C_{SC}^2} = \frac{2}{\varepsilon\varepsilon_0 e N_D}\left(E - E_{fb} - \frac{kT}{q}\right), \tag{3}$$

where C is capacitance, C_{SC} is space-charge capacitance, ε is dielectric constant, ε_0 is vacuum permittivity, e is electron charge, N_D is donor density, E is applied potential, E_{fb} is flat-band potential, k is the Boltzmann constant, T is absolute temperature, and q is elementary charge. A positive slope indicates n-type behaviour, and lower donor density indicates fewer electron-conducting donor defects in the product layer.

3. Results and Discussion

3.1 Corrosion loss and ultraviolet inhibition

Mass loss was negligible at 7 days, suggesting that the initial phase was dominated by fast formation of surface products instead of significant coating consumption. During $14 - 35$ days, the mass loss of dark exposed samples was larger than

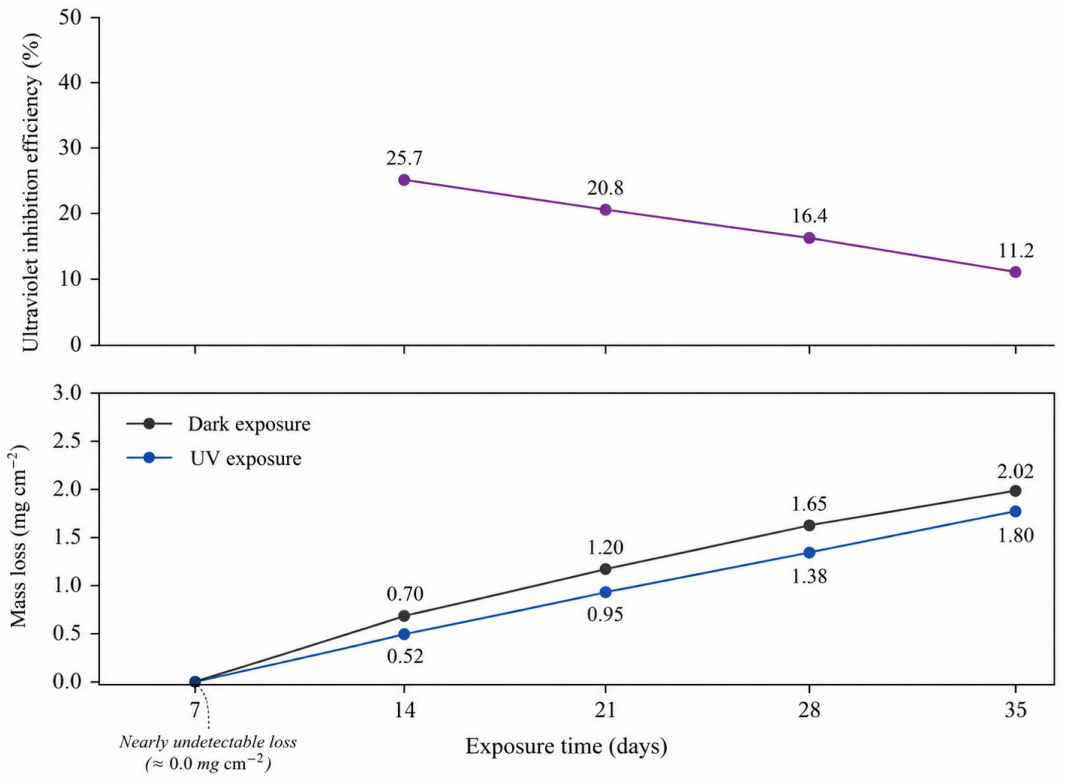


Figure 3: Mass loss and ultraviolet inhibition efficiency during exposure.

those of ultraviolet exposed samples. The figure below plots the relation between mass loss and inhibition effect, illustrating a decrease in the inhibition efficiency with time.

The data in Figure 3 indicates an ultraviolet inhibition decline from 25.7 % at 14 days to 20.8 % at 21 days, 16.4 % at 28 days and 11.2 % at 35 days. It suggests that the ultraviolet exposure accelerated the initial protective film formation, but could not avoid the further corrosion at the later exposure time. Under such circumstances, if there were a stable passive state due to illumination, a constant difference between dark and ultraviolet exposure would be observed or even increasing. However, the inhibition decline illustrates that the accumulated bisulfite deposition and thermal cycling resulted in the progressive deterioration of the dense film layer.

As for the results above, there seems to be a two-phase reaction on the surface. First, under the ultraviolet illumination, the surface product layer became more protective, possibly because of the formation of more compact hydroxy-sulfate film layer and less defect-induced transport. In the second phase, the repeated deposition of $NaHSO_3$ provided more availability of the sulfur species and acid environment, coupled with the thermal shock treatment, leading to the cracking of the film layer. Product conversion and cracking then open electrolyte pathways, which reduces the ultraviolet advantage at later exposure times.

3.2 Resistance polarization and protection effect by electrochemistry

The electrochemical impedance spectrum analysis verified that the resistance increase was non-monotonic for each exposure mode. Polarization resistance in Figure 4 revealed that ultraviolet exposure resulted in both a lower time of resistance peak emergence and a higher resistance peak value when compared with dark exposure. During the dark exposure, the polarization resistance R_p reached its peak value of $2.36 \times 10^4\,\Omega\ \mathrm{cm}^2$ on day 21. In contrast, during ultraviolet illumination, it reached its maximum value of $4.80 \times 10^4\,\Omega\ \mathrm{cm}^2$ on day 14.

The emergence of the resistance peak in Figure 4 indicated that the irradiation accelerated the appearance of the protective surface state. As the earlier emergence of the maximum resistance indicates the formation of such a barrier as that, the early emergence of resistance indicates the presence of a barrier that restrains transport processes in the product layer as well as interfacial charge-transfer processes. However, the decrease in resistance observed on day 35 of irradiation to $2.26 \times 10^3\,\Omega\ \mathrm{cm}^2$ indicated that the formed state was not stable in the conditions of bisulfite deposition and freeze-thaw cycles. Dark-exposed surface experienced the similar change in resistance on day 35, reaching $1.33 \times 10^3\,\Omega\ \mathrm{cm}^2$, which proves the loss of corrosion resistance of the corrosion product layer barrier.

The fitted resistance components identify the contribution of the product layer and the interface reactions. High R_r indicates the restriction of ionic conduction in the product layer, while high R_{ct} means the suppression of corrosion

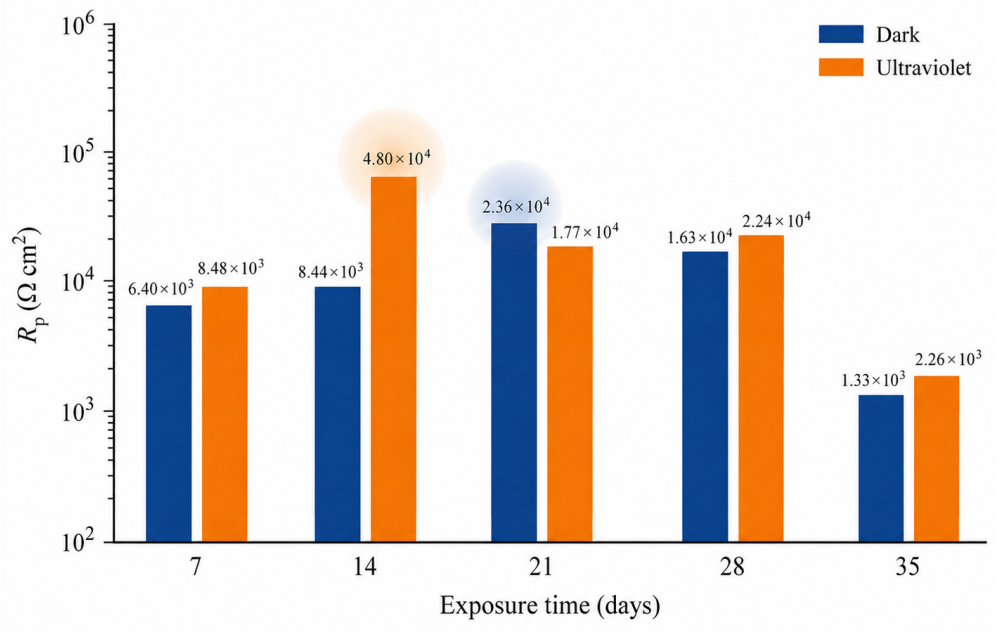


Figure 4: Polarization resistance evolution under dark and ultraviolet exposure.

reaction at the coating/electrolyte interface. Both factors were present in the case of ultraviolet condition at 14 days, where $R_r = 2.05 \times 10^4$ Ω cm^2 and $R_{ct} = 2.75 \times 10^4$ Ω cm^2. These results confirm the existence of an irradiated and effective product layer.

3.3 Short-term response to bisulfite deposition

In-situ impedance measurements provided information on the response to repeated $NaHSO_3$ deposition events. Measurements were carried out at 36, 72, 96, and 120 h, with a first $NaHSO_3$ deposition occurring at 0 h and a second one occurring at 84 h. As shown in Figure 5, the early polarization resistance response to repeated $NaHSO_3$ deposition demonstrated higher resistance during ultraviolet exposure in comparison to dark exposure within the entire monitored time frame.

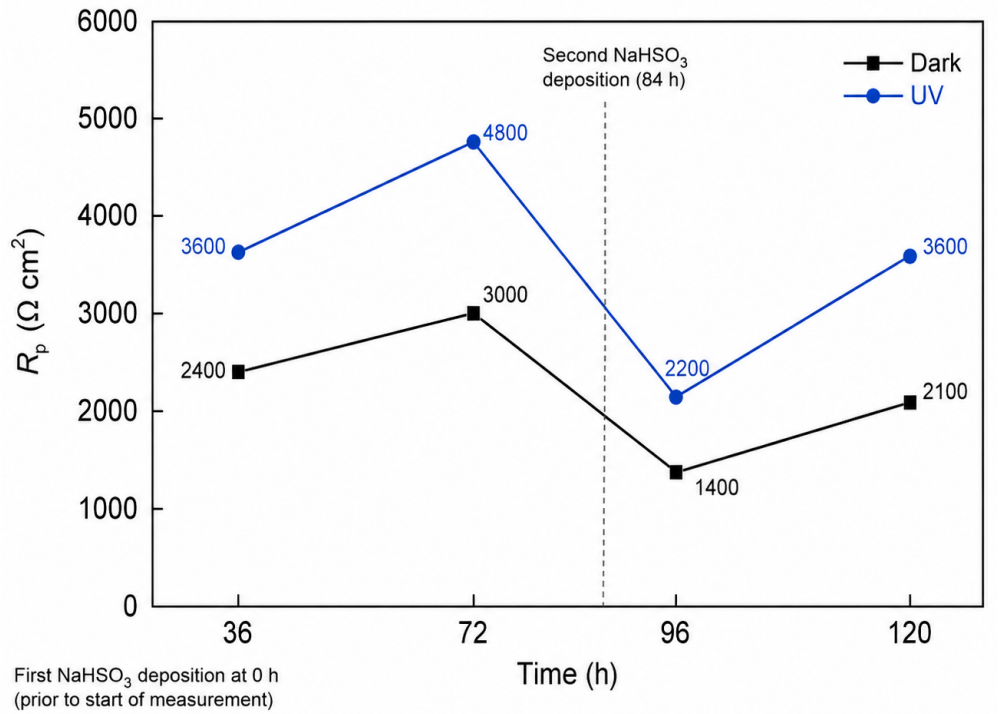


Figure 5: In-situ polarization resistance response to repeated $NaHSO_3$ deposition.

The data presented in Figure 5 indicate the rise of R_p from 36 to 72 h, drop after the second $NaHSO_3$ deposition, and partial recovery until 120 h. In particular, under ultraviolet exposure, R_p was growing from ~3600 to ~4800 Ω cm^2 before the second deposition, dropping to ~2200 Ω cm^2 at 96 h, and recovering back to ~3600 Ω cm^2 at 120 h. For the dark condition, similar behavior with lower resistance values was recorded.

The sudden drop in R_p after 84 h proves that $NaHSO_3$ depositions exert a chemical effect immediately. Indeed, the initial product layer containing rich concentrations of hydroxy-sulfates could be influenced by acidification and sulfite enrichment. Partial recovery after 120 h, in particular under ultraviolet illumination, supports the hypothesis of product layer reformation despite previous disturbances. Overall, these in-situ results support the idea of dynamism: ultraviolet exposure favors product layer recovery and compactness, while each $NaHSO_3$ deposition decreases its stability.

3.4 Phase evolution of the crystalline products

The XRD analysis did not reveal any new crystalline products due to ultraviolet illumination. Phase evolution in Figure 6 suggests similar main product species in dark and ultraviolet conditions with different ratios, which depend on time. For instance, at 7 days, two crystalline products ($Zn_4SO_4(OH)_6{\cdot}4H_2O$ and SiO_2) were identified. After 21 days, $Zn_2(SO_3)(SO_4){\cdot}3H_2O$ was formed for the dark condition, while $Zn_4SO_4(OH)_6{\cdot}4H_2O$ prevailed under ultraviolet exposure. $Zn_2(SO_3)(SO_4){\cdot}3H_2O$ prevailed on both surfaces by the end of day 35.

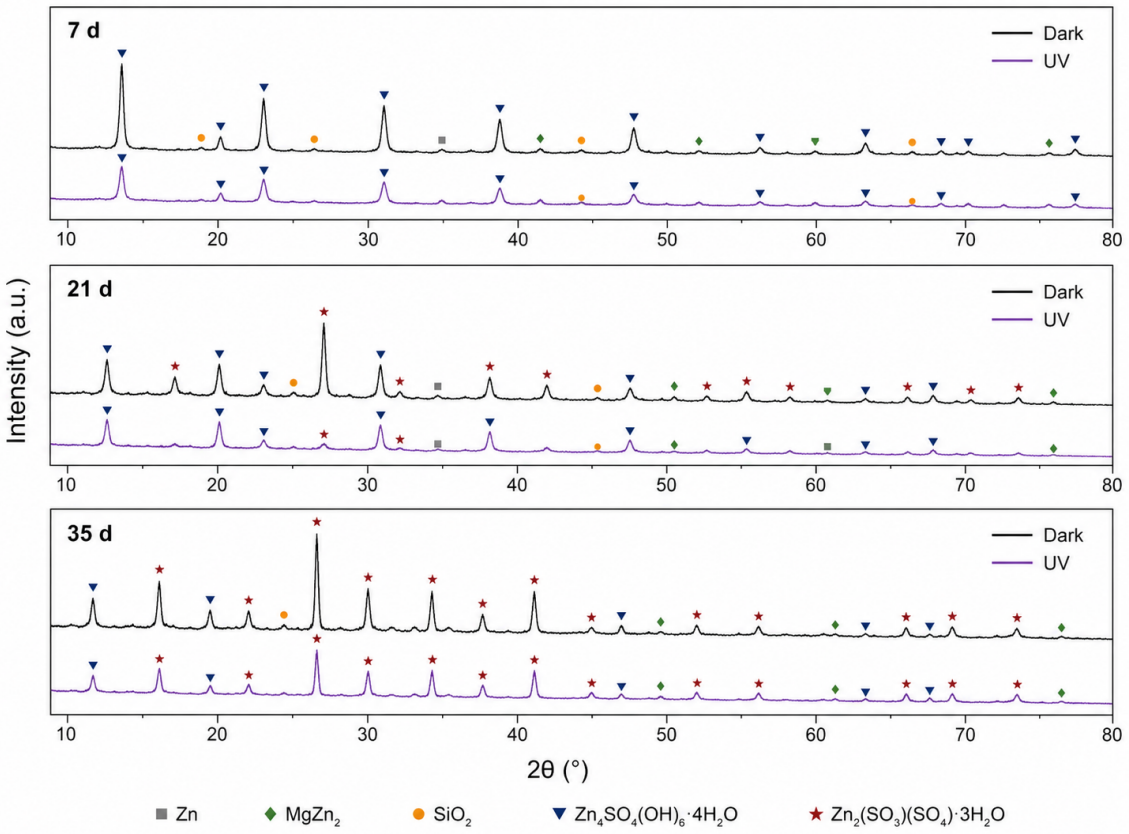


Figure 6: XRD phase evolution during dark and ultraviolet exposure.

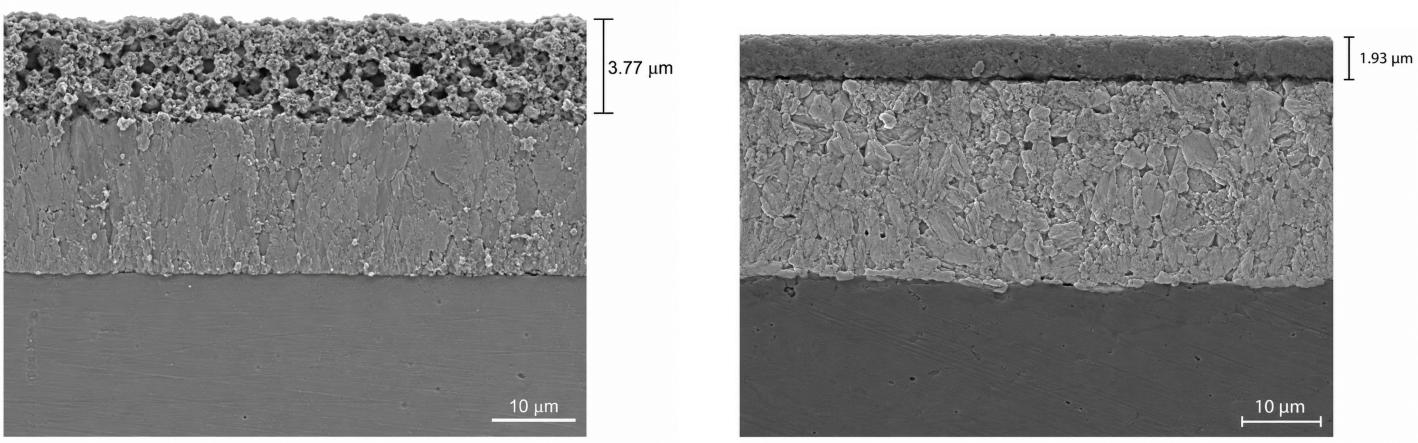
The explanation for the observed resistance behavior is evident from the phase evolution in Figure 6. It is worth noting that zinc hydroxysulfate ($Zn_4SO_4(OH)_6{\cdot}4H_2O$) corresponds to the initial protective stage, where a compact and moderately insoluble hydroxy-sulfate layer can form. The more pronounced appearance of $Zn_4SO_4(OH)_6{\cdot}4H_2O$ in ultraviolet samples up to day 21 corresponds to the better resistance achieved in the same period. The earlier emergence of $Zn_2(SO_3)(SO_4){\cdot}3H_2O$ under dark conditions suggests faster formation of a less protective product structure.

Figure 6 shows why the inhibition efficiency decreased at 35 days of exposure. In view of the fact that $Zn_2(SO_3)(SO_4){\cdot}3H_2O$ prevailed in both cases, there was little difference in phases deposited in dark and UV-treated environments. The additional inhibiting effect of ultraviolet rays consisted mainly in residual compact areas of the corrosion product. In other words, ultraviolet exposure contributed less to the crystallographic properties of the corrosion product. In addition, sodium bisulfite behaved contradictory to the corrosion protection mechanism – it provided an extra amount of sulfate required for early phase formation, but subsequent deposition resulted in increased acidity and sulfite-sulfate chemistry that favored late product formation.

3.5 Cross-sectional product compactness

Microscopy of cross-sections at day 7 clarified the reasons behind ultraviolet inhibition efficiency. The dark-exposed surface formed a corrosion product coating approximately 3.77 μm thick, whereas ultraviolet-exposed surface formed a thin layer

with the thickness of about 1.93 μm. Two paired cross-sections shown in Figure 7 clearly demonstrate that the former is porous and loose, while the latter is denser and more compact.



(a) Dark exposure, 7 days.

(b) Ultraviolet exposure, 7 days.

Figure 7: Early product-layer compactness after 7 days.

However, as seen in Figure 7, increased product thickness did not mean better protection. Increased porosity with connected pores in the thick product layer could facilitate the penetration of electrolyte and supply oxygen for corrosion. Thus, the 3.77 μm thick product layer after dark exposure is denser in terms of the volume of the product formed, yet lower in protective effect. On the other hand, a thinner product layer of 1.93 μm thick, formed upon ultraviolet exposure, exhibited superior protective properties due to greater compactness and lower interfacial activity.

These observations are consistent with both mass loss and impedance data. The protection effect achieved using ultraviolet exposure was not associated with the production of more corrosion products, but rather, an improvement in the quality of products. In other words, an increase in the compactness of the product layer resulted in a better resistance of the coating against corrosion since more efficient barrier properties were observed.

The enhanced compactness of the ultraviolet-exposed product layer is also in line with the lower donor density determined using the Mott–Schottky method.

3.6 Semiconductor defect density

Mott–Schottky plots obtained after 168 hours indicate positive values of the slope of the plots, proving the n-type semiconductor properties of the corrosion product layers. Figure 8 shows the plot depicting both the Mott–Schottky and donor density.

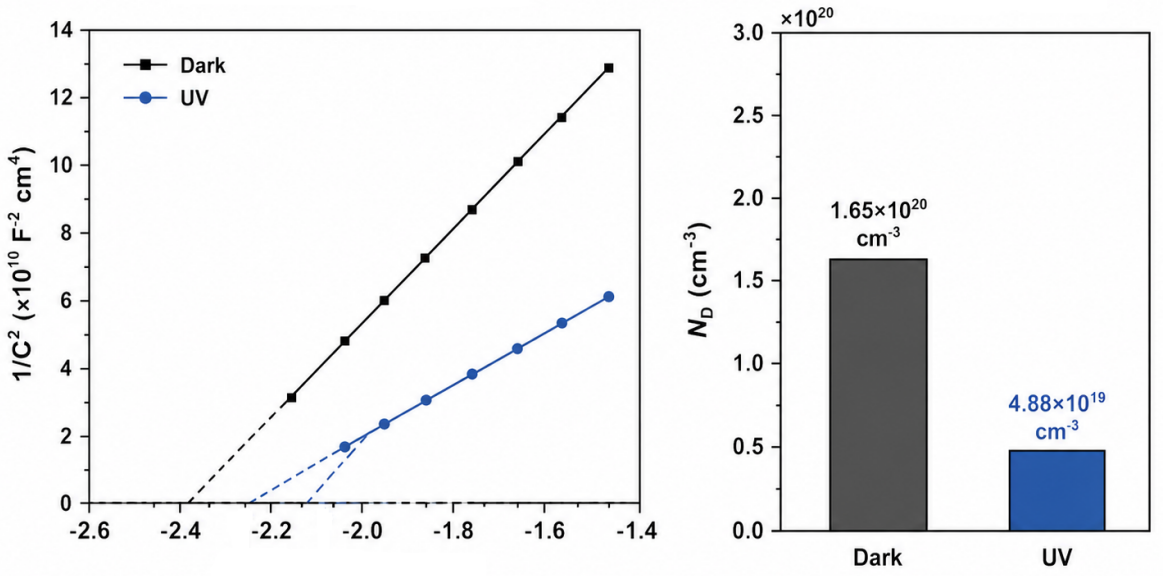


Figure 8: Mott–Schottky response and donor density comparison after 168 h.

Based on the Mott–Schottky plot shown in Figure 8, the decrease in donor density from 1.65×10^{20} cm^{-3} in the absence of ultraviolet illumination to 4.88×10^{19} cm^{-3} under ultraviolet illumination led to the shift in the value of the flat band

potential towards -1.99 V(SCE).

The reduction in donor density reflects the decrease in the concentration of electrically active donor defects. Hence, the formation of a layer of the corrosion products characterized by lower donor density results in a decrease in electronic conductivity. As a consequence, the effect of electronic interaction between anodic and cathodic reactions is minimized. Therefore, the Mott–Shottky curve confirms the results of impedance analysis and explains the higher values of impedance resistance caused by the decreased donor density.

3.7 Late-stage surface cracking

Late-stage surface topography after 35 days indicates the development of crack connections between corrosion products in both samples – exposed in the dark and irradiated with UV light. The comparison of surfaces with a developed corrosion layer after 35 days (Figure 9) reveals the occurrence of cracks on the surface in the dark condition and partial formation of a denser structure in ultraviolet exposure. However, cracks are also present in this case.

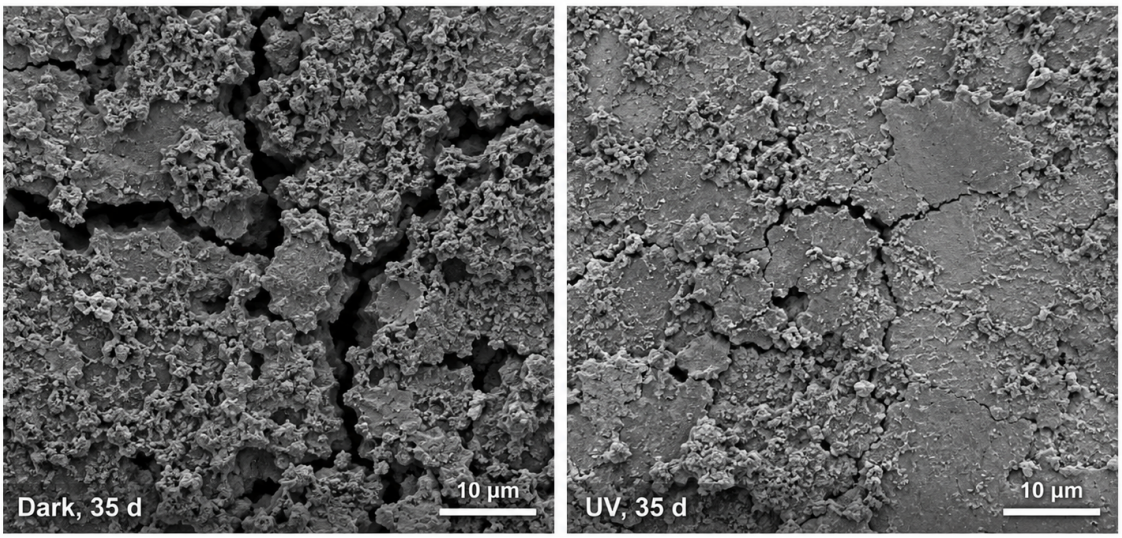


Figure 9: Late-stage surface morphology after 35 days.

This result explains why the inhibiting effect caused by the use of ultraviolet light weakened with the increase in exposure time. The presence of cracks provides electrolyte and oxygen transportation pathways, leading to a corrosion process proceeding at the interface between coating and product layer.

At the same time, once the cracks are formed, the protective effect related to the dense structure and high impedance of the product layer loses its importance, and the layer starts exhibiting reduced resistance. The irradiated sample exhibits higher impedance resistance at 35 days compared with the dark condition; however, the difference is much less than that observed earlier.

Cracking of the product layer occurs due to chemical and mechanical actions. The application of bisulfite leads to acidification and further sulfite–sulfate conversion and the development of corrosion reaction involving $Zn_2(SO_3)(SO_4)\cdot 3H_2O$ formation. Repeated thermal cycles with a temperature variation of $\Delta T = -60 - 20$ K produce stress affecting the corrosion products, causing cracks. In such a way, the corrosion product layer changes its properties from dense barrier into cracked one.

3.8 Integrated corrosion pathway

The anodic reaction in the sacrificial coating dissolving process is represented as follows:

$$Zn \rightarrow Zn^{2+} + 2e^{-}. \tag{4}$$

The cathodic reaction corresponds to the reduction of oxygen:

$$O_2 + 2H_2O + 4e^{-} \rightarrow 4OH^{-}. \tag{5}$$

The compact nature of the product layer reduces both anodic and cathodic reaction rates, restricting access of electrolyte and oxygen to the active interface. When cracks appear in the product layer, electrolyte and oxygen can diffuse inside the coating, thus increasing their activity.

Bisulfite oxidation results in the generation of sulfate and H^+ ions:

$$2HSO_3^- + O_2 \rightarrow 2SO_4^{2-} + 2H^+. \tag{6}$$

Sulfate ion is involved in the process of formation of $Zn_4SO_4(OH)_6{\cdot}4H_2O$:

$$4Zn^{2+} + SO_4^{2-} + 6OH^- + 4H_2O \rightarrow Zn_4SO_4(OH)_6 \cdot 4H_2O. \tag{7}$$

However, the development of acidity prevents this corrosion product from formation. At the same time, the following reaction proceeds resulting in sulfite ions and H^+:

$$HSO_3^- \rightarrow SO_3^{2-} + H^+, \tag{8}$$

and thus, a different product forms:

$$2Zn^{2+} + SO_4^{2-} + SO_3^{2-} + 3H_2O \rightarrow Zn_2(SO_3)(SO_4) \cdot 3H_2O. \tag{9}$$

4. Conclusions

Coating of steel substrate with Zn–Al–Mg alloy containing 20 μm thick layer and 4.4 wt.% Mg, 6.8 wt.% Al, 4.8 wt.% Si, 0.5 wt.% P, and the remaining Zn was investigated for 14 and 35 days at exposure temperatures of −60 and 20 °C, $NaHSO_3$ addition and ultraviolet illumination. Thus, the simultaneous action of thermal, humidity, chemical, and radiation stresses was examined with respect to extreme cold polluted atmosphere conditions.

Ultraviolet exposure reduced mass loss from 14 to 35 days from 135 to 67 mg, while inhibition efficiency was reduced from 25.7% to 11.2%. The decrease in the efficiency is explained by the fact that ultraviolet illumination improves protective abilities of the early stage corrosion product layer, but does not prevent its destruction during further treatment.

Electrochemical impedance spectroscopy revealed the acceleration of the most protective surface state formation under irradiation. The maximum resistance was recorded for the dark sample (2.36×10^4 Ω cm^2) on day 21. However, in the case of ultraviolet illumination, the corresponding maximum was detected at day 14 (4.80×10^4 Ω cm^2), and then significantly lowered.

XRD analysis did not reveal new phases in the product layer upon UV illumination. The early layer consisted of $Zn_4SO_4(OH)_6{\cdot}4H_2O$, while the $Zn_2(SO_3)(SO_4){\cdot}3H_2O$ product prevailed in the long-term treatment. Nevertheless, ultraviolet illumination extended the period of $Zn_4SO_4(OH)_6{\cdot}4H_2O$ dominance in the layer composition.

Cross-sectional micrographs indicated that the product compactness was more important than its thickness. While the dark exposed layer had a thickness of 3.77 μm, the ultraviolet one was only 1.93 μm thick but denser. Thus, the thinner compact layer was more effective in protection than the thick one.

Mott-Schottky revealed n-type semiconductors behavior. Donor concentration reduced from 1.65×10^{20} cm^{-3} in the dark to 4.88×10^{19} cm^{-3} upon ultraviolet light illumination, and the flat-band voltage increased from −2.09 to −1.99 V(SCE). This indicates less number of defects as electrically active in the layer formed upon irradiation, and therefore more resistance and dense morphology.

The corrosion mechanism starts with formation of the protective layer due to ultraviolet exposure, followed by sulfate-sulfite transformation and cracking because of freeze/thaw action caused by $NaHSO_3$. After cracks are formed in the surface barrier, electrolyte penetration takes place, resulting in diminishing role of the first step of the process.

References

[1] Volovitch, P., Vu, T. N., Allély, C., Aal, A. A., & Ogle, K. (2011). Understanding corrosion via corrosion product characterization: II. Role of alloying elements in improving the corrosion resistance of Zn–Al–Mg coatings on steel. Corrosion Science, 53(8), 2437-2445.

[2] Schürz, S., Luckeneder, G. H., Fleischanderl, M., Mack, P., Gsaller, H., Kneissl, A. C., & Mori, G. (2010). Chemistry of corrosion products on Zn–Al–Mg alloy coated steel. Corrosion Science, 52(10), 3271-3279.

[3] Prosek, T., Larché, N., Vlot, M., Goodwin, F., & Thierry, D. (2010). Corrosion performance of Zn–Al–Mg coatings in open and confined zones in conditions simulating automotive applications. Materials and Corrosion, 61(5), 412-420.

[4] Prosek, T., Persson, D., Stoulil, J., & Thierry, D. (2014). Composition of corrosion products formed on Zn–Mg, Zn–Al and Zn–Al–Mg coatings in model atmospheric conditions. Corrosion Science, 86, 231-238.

[5] Diler, E., Rouvellou, B., Rioual, S., Lescop, B., Vien, G. N., & Thierry, D. (2014). Characterization of corrosion products of Zn and Zn–Mg–Al coated steel in a marine atmosphere. Corrosion Science, 87, 111-117.

[6] Thierry, D., Persson, D., Luckeneder, G., & Stellnberger, K. H. (2019). Atmospheric corrosion of ZnAlMg coated steel during long term atmospheric weathering at different worldwide exposure sites. Corrosion Science, 148, 338-354.

[7] Azevedo, M. S., Allély, C., Ogle, K., & Volovitch, P. (2015). Corrosion mechanisms of Zn (Mg, Al) coated steel in accelerated tests and natural exposure: 1. The role of electrolyte composition in the nature of corrosion products and relative corrosion rate. Corrosion Science, 90, 472-481.

[8] Azevedo, M. S., Allély, C., Ogle, K., & Volovitch, P. (2015). Corrosion mechanisms of Zn (Mg, Al) coated steel: 2. The effect of Mg and Al alloying on the formation and properties of corrosion products in different electrolytes. Corrosion Science, 90, 482-490.

[9] Gu, T., Liu, Y., Peng, C., Zhang, P., & Wang, Z. (2022). Initial atmospheric corrosion of zinc-aluminum-magnesium coated steel and galvanized steel in regions of extremely cold and industrial climate. Materials Chemistry and Physics, 291, 126686.
[10] Graedel, T. E. (1989). Corrosion mechanisms for zinc exposed to the atmosphere. Journal of the Electrochemical Society, 136(4), 193C-203C.
[11] Veleva, L., Meraz, E., & Acosta, M. (2007). Zinc corrosion runoff process induced by humid tropical climate. Materials and Corrosion, 58(5), 348-352.
[12] Cole, I. S. (2017). Recent progress and required developments in atmospheric corrosion of galvanised steel and zinc. Materials, 10(11), 1288.
[13] Leygraf, C. (2002). Atmospheric corrosion. In Corrosion mechanisms in theory and practice (pp. 538-571). CRC Press.
[14] Mikhailov, A. A., Strekalov, P. V., & Panchenko, Y. M. (2008). Atmospheric corrosion of metals in regions of cold and extremely cold climate (a review). Protection of Metals, 44(7), 644-659.
[15] Choi, Y. Y., & Kim, M. H. (2018). Corrosion behaviour of welded low-carbon steel in the Arctic marine environment. RSC advances, 8(53), 30155-30162.
[16] Momber, A. W., Irmer, M., Glück, N., & Plagemann, P. (2016). Corrosion protection performance of organic offshore coating systems at −60 °C temperature shock. *Journal of Offshore Mechanics and Arctic Engineering*, 138(6), 064501.
[17] Odnevall, I., & Leygraf, C. (1994). The formation of Zn4SO4 (OH) 6 · 4H2O in a rural atmosphere. Corrosion science, 36(6), 1077-1087.
[18] Ligier, V., Wéry, M., Hihn, J. Y., Faucheu, J., & Tachez, M. (1999). Formation of the main atmospheric zinc end products: $NaZn_4Cl(OH)_6SO_4 \cdot 6H_2O$, $Zn_4SO_4(OH)_6 \cdot nH_2O$ and $Zn_4Cl_2(OH)_4SO_4 \cdot 5H_2O$ in $[Cl^-][SO_4^{2-}][HCO_3^-][H_2O_2]$ electrolytes. *Corrosion Science*, 41(6), 1139–1164.
[19] Persson, D., Prosek, T., LeBozec, N., Thierry, D., & Luckeneder, G. (2015). Initial SO2-induced atmospheric corrosion of ZnAlMg coated steel studied with in situ Infrared Reflection Absorption Spectroscopy. Corrosion Science, 90, 276-283.
[20] Xu, Y., & Schoonen, M. A. (2000). The absolute energy positions of conduction and valence bands of selected semiconducting minerals. American mineralogist, 85(3-4), 543-556.
[21] Kalinauskas, P., Valsiūnas, I., & Juzeliūnas, E. (2001). Zinc photo-corrosion in neutral solutions. Corrosion science, 43(11), 2083-2092.
[22] Song, L., Ma, X., Chen, Z., & Hou, B. (2014). The role of UV illumination on the initial atmospheric corrosion of 09CuPCrNi weathering steel in the presence of NaCl particles. Corrosion Science, 87, 427-437.
[23] Breslin, C. B., Macdonald, D. D., Sikora, J., & Sikora, E. (1997). Influence of uv light on the passive behaviour of SS316—effect of prior illumination. Electrochimica acta, 42(1), 127-136.
[24] Schmuki, P., & Böhni, H. (1995). Illumination effects on the stability of the passive film on iron. Electrochimica Acta, 40(6), 775-783.
[25] Moussa, S. O., & Hocking, M. G. (2001). The photo-inhibition of localized corrosion of 304 stainless steel in sodium chloride environment. Corrosion science, 43(11), 2037-2047.
[26] Stoulil, J., Prosek, T., Nazarov, A., Oswald, J., Kriz, P., & Thierry, D. (2015). Electrochemical properties of corrosion products formed on Zn-Mg, Zn-Al and Zn-Al-Mg coatings in model atmospheric conditions. Materials and Corrosion, 66(8), 777-782.
[27] ISO, N. (2021). 8407: 2021; Corrosion of Metals and Alloys—Removal of Corrosion Products from Corrosion Test Specimens. International Organization for Standardization (ISO): Geneva, Switzerland.